Polar magneto-optical Kerr effect in antiferromagnetic M_2As (M = Cr, Mn, Fe) under an external magnetic field

Kisung Kang,[1] Kexin Yang,[2] Krithik Puthalath,[1,2] David G. Cahill,[1,2,3] and André Schleife[1,3,4,*]

[1]*Department of Materials Science and Engineering, University of Illinois at Urbana-Champaign, Urbana, Illinois 61801, USA*
[2]*Department of Physics, University of Illinois at Urbana-Champaign, Urbana, Illinois 61801, USA*
[3]*Materials Research Laboratory, University of Illinois at Urbana-Champaign, Urbana, Illinois 61801, USA*
[4]*National Center for Supercomputing Applications, University of Illinois at Urbana-Champaign, Urbana, Illinois 61801, USA*

(Received 4 December 2020; revised 3 January 2022; accepted 6 April 2022; published 2 May 2022)

Antiferromagnetic (AFM) metals have attracted tremendous interest for memory applications due to their expected fast response dynamics in the terahertz frequency regime. Spin dynamics such as AFM resonance and the magnon relaxation rate have been measured using the linear magneto-optical Kerr effect (MOKE) with coherent spin precession induced by laser pumping. Polarized electromagnetic radiation is a promising alternative for probing the response in canted AFM systems. Hence, in this paper, we use first-principles simulations to study the magneto-optical response of AFM M_2As (M = Cr, Mn, and Fe) under external magnetic fields. We devise a computational scheme to compute the magnetic susceptibility from total-energy changes using constraints on magnetic-moment tilting. Our predictions of the spectral dependence of polar magneto-optical Kerr rotation and ellipticity allow us to attribute these effects to breaking of the magnetic symmetry. We show that tilting of magnetic moments affects the exchange interaction, while the spin-orbit interaction remains unaffected. In this paper, we provide an understanding of the polar MOKE on a band structure level and underscore the importance of the magnetic susceptibility when searching for materials with large magneto-optical response.

DOI: 10.1103/PhysRevB.105.184404

I. INTRODUCTION

As society becomes increasingly data driven, the ability to store and access large amounts of information quickly has become of utmost importance, keeping up with the growing global demand for high-performance electronics. Random access memory [1], used in computing devices, has seen tremendous growth owing to giant magnetoresistance. Spin valves have paved the way for the development of magnetic random access memory based on magnetotunneling resistance [2]. However, the magnitude of the anisotropy field in ferromagnetic (FM) materials limits the response dynamics to the gigahertz range.

Antiferromagnetic (AFM) materials are currently attracting tremendous interest [3] since they may overcome some of these limitations: Due to the strong exchange interaction between sublattice magnetic moments, AFMs are expected to have fast response dynamics in the terahertz frequency regime. Additionally, unlike FM materials, AFMs exist in each magnetic symmetry group, providing a vast space of magnetic-moment configurations [4]. Hence, there is a large number of candidate AFMs, and they are ubiquitous in the form of metals, semi-metals, insulators, and superconductors [4]. However, in AFM materials, the characterization of the magnetic structure requires large-scale facilities for neutron diffraction or synchrotron x-ray measurement. Thus, it is important to develop a tabletop setting experiment to detect the magnetic structure and spin dynamics.

In addition, AFMs show faint high-order magneto-optical signals and have a robust magnetic structure against external fields. In contrast to FM materials, where the magnetic moments are aligned in a preferential easy-axis direction, collinear AFMs exhibit alternating magnetic moments, and noncollinear AFMs exhibit more complex magnetic moment geometries throughout the lattice, resulting in vanishing net magnetization. While this is the origin of the robustness of AFMs to external magnetic fields, which allows them to withstand interference from deleterious stray fields, it also renders them invisible to magnetic probes.

Polarized electromagnetic radiation is a promising alternative probe of material response [5], suitable for characterization of spin dynamics of AFMs through a tabletop laboratory experiment [6]. The magneto-optical Kerr effect (MOKE) [7] has been used to probe electronic and magnetic properties by measuring the polarization rotation of reflected light under various geometries. From a response function point of view, the linear MOKE for collinear AFMs is related to the first-order term of an expansion of the dielectric tensor into increasing orders of net magnetization and the Néel vector [3,8–11]. Oppeneer *et al.* [12] showed for FMs that the nonvanishing linear MOKE requires the presence of both spin-orbit coupling (SOC) and exchange splitting in a material. However, due to the vanishing net magnetization, majority and minority spin states are degenerate in collinear AFMs; hence, exchange splitting is absent. To use the linear MOKE to study collinear AFMs, one of the simplest approaches is to apply an

*schleife@illinois.edu

external magnetic field to generate a small net magnetization along the field direction. The linear MOKE can then be distinguished into polar, longitudinal, and transversal geometry, depending on whether the net magnetization is oriented perpendicular to the sample surface, lies in the sample surface and in the plane of incidence, or lies in the sample surface and perpendicular to the plane of incidence, respectively. In this paper, we focus on the polar MOKE (PMOKE). The PMOKE is combined with time-resolved measurements to extract the temperature-dependent spin-wave frequency and its damping rate for AFM NiO [13]. When the laser pump excites AFM NiO, coherent spin precession with the tilting and oscillating PMOKE signals is induced, providing resonance frequency and relaxation time [13].

We perform first-principles simulations using density functional theory (DFT) to study the ground and moment-tilted states of AFM M_2As (M = Cr, Mn, and Fe). Due to their high Néel temperatures above room temperature of 393 K [14], 573 K [15], and 353 K [16], respectively, these materials have potential for utilization in spintronic devices at room temperature. Moment tilting is imposed in our first-principles approach to account for the effect of an external magnetic field acting on M_2As, and we compute the magnetic susceptibility from the resulting change in total energy. We also perform first-principles simulations to investigate the PMOKE signal for light incidence parallel to the c axis. Finally, we discuss the SOC effect and exchange splitting in the electronic band structure for the ground and spin-tilted states to unveil the origin of our reported Kerr rotation and ellipticity spectra. We note that all units in this paper are in SI unless otherwise noted explicitly.

II. COMPUTATIONAL APPROACH

We perform fully relativistic, noncollinear first-principles DFT [17] simulations using the Vienna *Ab Initio* Simulation Package (VASP) [18–21]. We also compute and compare magnetic susceptibilities for MnPt [22], tetragonal CuMnAs, Mn_2Au, Cr_2Al [23], Mn_3Sn, and MnF_2. In all calculations, we account for noncollinear magnetization and consider SOC [21]. The generalized-gradient approximation as parameterized by Perdew, Burke, and Ernzerhof [24] is used to describe exchange and correlation. Kohn-Sham states are expanded into a plane-wave basis with a kinetic energy cutoff of 600 eV. A $15 \times 15 \times 5$ Monkhorst-Pack (MP) grid [25] was used for Brillouin zone sampling for all M_2As materials. We used a $15 \times 15 \times 15$ MP grid for MnPt [22], a $18 \times 18 \times 10$ MP grid for tetragonal CuMnAs, a $18 \times 18 \times 7$ MP grid for Mn_2Au, a $21 \times 21 \times 7$ MP grid for Cr_2Al [23], a $16 \times 16 \times 20$ Γ-centered grid for Mn_3Sn, and a $16 \times 16 \times 24$ MP grid for MnF_2. Convergence tests showed that this leads to an accuracy within 0.01 meV/f.u. for the total energy. To accelerate self-consistent minimization of the metallic electronic ground state of these materials, we used Gaussian smearing of 25 meV in all calculations. In addition, for MnF_2, we perform DFT + U simulations for an accurate electronic structure description based on the method developed by Dudarev *et al.* [26] with an onsite Coulomb parameter $U = 4.9$ eV and an exchange parameter $J = 1.0$ eV, as selected in the preceding work of López-Moreno *et al.* [27]. For Mn_2Au and CuMnAs, we also use the DFT + U approach with the method of Dudarev *et al.* [26] and effective onsite Coulomb parameters of $U_{\text{eff}}^{\text{Mn}_2\text{Au}} = U - J = 1.4$ eV and $U_{\text{eff}}^{\text{CuMnAs}} = 1.3$ eV that closely reproduce the experimentally reported chemical and magnetic structure.

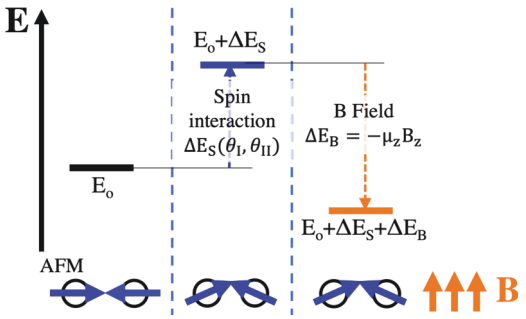

FIG. 1. Total energy schematic for the antiferromagnetic (AFM) ground state E_0, the spin-tilted configuration $E_0 + \Delta E_S$, and considering an external magnetic field B as the origin of the tilting. The spin-tilted state has higher energy with respect to the ground state because of spin-spin interaction energy (ΔE_S); an external magnetic field can lower its total energy (ΔE_B). These energies are a function of sublattice magnetization along the z axis (μ_z).

The magnetic moments of a material can tilt perpendicularly to the AFM configuration in response to an external magnetic field (see Fig. 1). To implement the magnetic moment tilting, the magnitude of each magnetic moment was fully relaxed, but its direction was strongly constrained. This is achieved in VASP by introducing an energy penalty term so that the total energy becomes

$$E = E_0 + \sum_I \lambda \left[\mathbf{M}_I - \mathbf{M}_I^0 \left(\mathbf{M}_I^0 \cdot \mathbf{M}_I\right)\right]^2. \tag{1}$$

The sum runs over all sites I, $\mathbf{M}_I^0$ is the direction of the constraint at each atomic site, and $\mathbf{M}_I$ is the integrated magnetic moment at site I [28]. We used $\lambda = 50$ for the penalty parameter in this paper and verified that this choice maintains the imposed moment tilting. The energy penalty term, in this case, amounts to ∼0.3 μeV for tilting of 10°. This tilting also changes the magnetic order and breaks the magnetic symmetry of the material, leading to a net magnetization along the field direction. For each of these tilted states, we compute lattice parameters and atomic geometries by minimizing Hellman-Feynman forces.

Tilting of AFM coupled moments against their antiparallel configuration, i.e., along the field orientation but perpendicular to the easy plane or easy axis, is accompanied by an exchange energy penalty and energy decrease due to Zeeman energy. While most materials studied in this paper have only one magnetic site, the magnetic moments of the two different magnetic sites in M_2As can tilt with different angles. Thus, we study states with both angles θ_{I} and θ_{II} simultaneously tilting from 0° to 10° in 1° increments and, in addition, varying θ_{I} at the $M(I)$ site, while keeping $\theta_{\text{II}} = 10°$ at the $M(II)$ site.

From our DFT simulations, we obtain total energies of the AFM ground states E_0 as well as total energies of the different moment-tilted configurations $E_0 + \Delta E_S(\theta_{\text{I}}, \theta_{\text{II}})$ (see Fig. 1) to construct the corresponding total energy surface for

both angles. We then fit a model for $E_0 + \Delta E_S(\theta_I, \theta_{II})$ to the DFT data, based on the spin-spin interaction described via an exchange term due to the induced sublattice magnetization, ignoring classical dipole-dipole contributions. It originates from the exchange interaction terms ($J_{ij}S_iS_j$), where S_i is the magnetic moment vector at site i, and thus, it is proportional to the square of magnetic moments, resulting in a paraboloid energy surface in terms of θ_I and θ_{II}. We then account for the energy $\Delta E_B(\theta_I, \theta_{II})$ of a magnetic moment due to the net magnetization in an external magnetic field. This allows us to express the total energy as

$$E_{tot} = E_0 + \Delta E_S(\theta_I, \theta_{II}) + \Delta E_B(\theta_I, \theta_{II}). \tag{2}$$

To compute the magnetic susceptibility, we investigate the total energy with varying angles from DFT calculations to find the energy surface by the paraboloidal fitting. The relationship between E_{tot} and the net magnetization μ_z along the field direction is crucial to evaluate the ground state energy under each external magnetic field. The net magnetization μ_z can be defined by the z component of the total magnetization created by the tilting with θ_I and θ_{II}, i.e., $\mu_z(\theta_I, \theta_{II})$. Within the linear response regime, we assume the relative ratio between two angles is fixed as $d = \theta_{II}/\theta_I$. In the Supplemental Material [29], we derive a relationship between the z component of the sublattice magnetization μ_z and the external magnetic field:

$$B_z = 2\xi_{min}\mu_z, \tag{3}$$

where ξ_{min} represents the curvature of the energy curve as a function of net magnetization minimizing the total energy change (ΔE_S) from the ground state energy (E_0) under the magnetic field. It can be computed by the derivative of the curvature in terms of the angle ratio d (see Eq. (S9) and details in the Supplemental Material [29]). Combining with the definition of the magnetic susceptibility,

$$B = \mu_0(M + H) = \mu_0(1 + \chi_v)H, \tag{4}$$

we find

$$\chi_v = \frac{\mu_0}{2\xi_{min} - \mu_0}, \tag{5}$$

where μ_0 is the vacuum permeability.

After we find the tilted magnetic structure for each magnetic field, we subsequently compute the frequency-dependent complex dielectric tensor [20]. We use the Kohn-Sham eigenvalues and single-particle states to study the electronic band structure and to compute the complex, frequency-dependent dielectric tensors of M_2As, including the anomalous Hall conductivity (AHC) contribution [30], using the VASP code [20]. We note that Drude-like intraband contributions in the low-energy range of the frequency-dependent dielectric tensors are not included in our simulations. This is because, in magneto-optical spectra from experiments on CuMnAs [31] and Fe [30], these contributions are reported to be confined to the energy range <1.0 eV, which is less than the visible light spectral range that is the focus of this paper. From the diagonal and off-diagonal components of the dielectric tensor, we compute complex PMOKE signals using [30]

$$\Psi_K(\omega) = \theta_K(\omega) + i\gamma_K(\omega) = \frac{-\epsilon_{xy}}{(\epsilon_{xx} - 1)\sqrt{\epsilon_{xx}}}. \tag{6}$$

Within the Ehrenreich-Cohen approach [32], the complex, frequency-dependent dielectric function follows from a sum over valence-conduction electronic transitions, where each transition is weighted by the corresponding dipole matrix element. This allows us to decompose our computed optical spectra by projecting valence or conduction electronic states on atomic orbitals. To this end, we use the following expression for the imaginary part of the dielectric function that is implemented in the VASP code and add the projection onto atomic orbitals, as described in Ref. [33], leading to

$$\varepsilon_{\alpha,\beta}(\omega) = \frac{4\pi e^2\hbar^2}{m^2}\sum_{uwk}\left(\sum_{N,l,m} P^N_{lmnk}\right) \times \left[\frac{\left(p^\alpha_{wuk}\right)^* p^\beta_{wuk} f_{uk}(1 - f_{wk})}{\hbar\omega - (\epsilon_{wk} - \epsilon_{uk})} - \frac{\left(p^\alpha_{uwk}\right)^* p^\beta_{uwk} f_{uk}(1 - f_{wk})}{\hbar\omega + (\epsilon_{wk} - \epsilon_{uk})}\right], \tag{7}$$

where ϵ_{wk} and ϵ_{uk} are the Kohn-Sham eigenvalues of band index w and u at **k**-point k with occupation numbers f_{wk} and f_{uk}, and p^α_{wuk} is the Cartesian α direction of the dipole matrix element for this transition. Here, P^N_{lmnk} is the projection of a Kohn-Sham state ϕ_{nk} on an orbital of atom N with orbital angular momentum l, magnetic quantum number m, and a band index n that can be either u or w. The real part follows from the Kramers-Kronig transformation.

In addition, we found that the AHC contribution to the dielectric function can also be decomposed into different projected orbitals:

$$\varepsilon^{AHC}_{\alpha,\beta}(\omega) = \frac{\hbar e^2}{2\pi^2 m^2\omega}\sum_{vwk}\left(\sum_{N,l,m} P^N_{lmnk}\right) \times (f_{uk} - f_{wk})\frac{\left(p^\alpha_{wuk}\right)^* p^\beta_{wuk}}{(\epsilon_{wk} - \epsilon_{uk})^2}. \tag{8}$$

The total decomposed dielectric function is the sum of the decomposed interband transition and decomposed AHC contribution. We then analyze our PMOKE results by decomposing only the off-diagonal component of the dielectric tensor, regarding their contribution from different orbitals and atoms:

$$\theta_K(\omega) + i\gamma_K(\omega) = \frac{-\varepsilon^s_{xy}}{(\varepsilon_{xx} - 1)\sqrt{\varepsilon_{xx}}} + \frac{-\varepsilon^p_{xy}}{(\varepsilon_{xx} - 1)\sqrt{\varepsilon_{xx}}} + \frac{-\varepsilon^d_{xy}}{(\varepsilon_{xx} - 1)\sqrt{\varepsilon_{xx}}}, \tag{9}$$

where ε^s_{xy}, ε^p_{xy}, and ε^d_{xy} are the decomposed off-diagonal components for s, p, or d orbitals, respectively. In the denominator, we used the nondecomposed diagonal component to maintain additivity.

III. RESULTS AND DISCUSSION

A. Atomic geometries

The atomic and magnetic structures of Cr_2As, Mn_2As, and Fe_2As in the magnetic ground state are shown in Fig. 2.

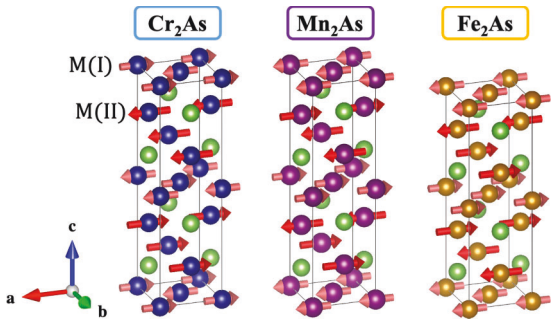

FIG. 2. Chemical and magnetic structure of Cr_2As, Mn_2As, and Fe_2As shown for the magnetic primitive unit cells. Chromium atoms are blue, manganese are purple, iron are gold, and arsenic are green. Magnetic cations of type I and II, M(I) and M(II), are chemically and magnetically nonequivalent and are indicated by the light and dark color of red arrows, respectively.

Lattice parameters and magnetic moments, computed from fully relaxed atomic geometries using DFT, are listed in Table I. The easy axis is defined as the Néel vector along the direction where the total energy becomes the lowest. The space group of the chemical structure is P_4/nmm for all three materials. While the magnetic ordering differs for the three M_2As compounds, all magnetic space and point groups are the same, P_anma and $mmm1'$, respectively. Tilting the magnetic moments changes the magnetic structure and breaks this symmetry: The magnetic space and point groups then become $Pnm'a$ and $m'm'm$. We identified all chemical and magnetic symmetries using FINDSYM in the ISOTROPY Software Suite [34,35], and from comparing all symmetry operations, we find that tilting of the magnetic moments breaks time reversal symmetry (T: $+1 \rightarrow -1$), thus enabling these M_2As materials to exhibit PMOKE signals.

TABLE I. Lattice parameters (in Å) and (untilted) magnetic moments (in μ_B) for Cr_2As, Mn_2As, and Fe_2As, compared with experimental values. Relative deviation from experimental values is given as Δ_{exp}. All experimental values are measured at room temperature, while the magnetic moments of Fe_2As in parentheses are extrapolated to 0 K, based on temperature-dependent measurements. Tilting of magnetic moments by 10° influences the lattice parameters by <0.1%.

Cr_2As	a	b	c	$\mu_{Cr(I)}$	$\mu_{Cr(II)}$
This paper	3.56	3.59	12.63	1.11	1.98
Exp. [14]	3.60	3.60	12.68	0.4	1.34
Δ_{exp} (%)	−0.8	0.1	−0.5	178	47.8
Mn_2As	a	b	c	$\mu_{Mn(I)}$	$\mu_{Mn(II)}$
This paper	3.68	3.68	12.27	1.87	3.24
Exp. [15]	3.78	3.78	12.56	3.70	3.50
Δ_{exp} (%)	−2.7	−2.7	−2.3	−49.5	−7.4
Fe_2As	a	b	c	$\mu_{Fe(I)}$	$\mu_{Fe(II)}$
This paper	3.624	3.624	11.72	1.23	2.25
Exp. [16]	3.627	3.627	11.96	0.95 (1.28)	1.52 (2.05)
Δ_{exp} (%)	−0.1	−0.1	−2.0	29.5 (−3.9)	95.3 (9.8)

Comparison with literature data shows that our results for lattice parameters agree to within 3% or better with experiment [14–16]. The large discrepancy for the amplitude of the magnetic moments of Cr_2As and Fe_2As (see Table I) can be explained by the experiments at room temperature, i.e., close to the corresponding Néel temperatures. Katsuraki and Achiwa [16] extrapolate the magnetic moment to 0 K based on the magnetic intensity from neutron scattering, which shows agreement within 10% of our simulations. For Mn_2As, the measured magnetic moment is larger than our calculated results. Similar calculations for Mn_2As are reported by Zhang *et al.* [36] and point out that this deviation originates from the lack of onsite Coulomb interaction of localized electrons.

B. Magnetic susceptibilities

The magnetic susceptibility is important to understand the response of the magnetic structure of AFM materials to external magnetic fields. It determines the orientation change of the magnetic moments in the material for a given applied external magnetic field, as discussed in Sec. II. In this paper, we focus on the case with an external field along a perpendicular direction to the Néel vector because magnetic susceptibility along that direction is large, and thus, it is expected to have the largest PMOKE signals. Magnetic susceptibility measurements were performed by Yuzuri [37] on polycrystalline $Cr_{2.1}As$ and Yuzuri and Yamada [38] on polycrystalline $Mn_{2.3}As$. The measured magnetic susceptibility of polycrystalline materials corresponds to a directional average. The polycrystalline measurements report that the unitless magnetic susceptibility of $Cr_{2.1}As$ [37] is 6.44×10^{-4} at 273 K and of $Mn_{2.3}As$ [38] is 1.23×10^{-3} at 465 K. Ishizawa and Hirahara [39] studied the magnetic susceptibility of a Mn_2As single crystal, resulting in $\chi_{\perp c} = 1.08 \times 10^{-3}$ at 364 K and $\chi_{\parallel c} = 9.42 \times 10^{-3}$ at 389 K along two different directions in terms of the c axis. For Fe_2As, the susceptibility was measured along the two different directions a (χ_a) and c (χ_c), see Fig. 2, of a single-crystalline sample, corresponding to the [100] and [001] directions [40]. The magnetic susceptibility of Fe_2As along the a and c axes is 6.96×10^{-3} at 263 K and 8.83×10^{-3} at 300 K, respectively [40]. The experimentally observed temperature-dependent magnetic susceptibility data of single crystalline Mn_2As [39] and Fe_2As [40] show a large increase with cooling. This does not follow the temperature-dependent behavior of the magnetic susceptibility expected for typical AFMs, which shows only a small variation of $\chi_\perp$ below the Néel temperature [41,42]. The physical origin of this unexpected behavior has not been clearly uncovered, and we attribute this unexpected behavior to the off-stoichiometry of the sample, paramagnetic impurities, or site disorder.

In Fig. 3, we illustrate the change in total energy ΔE_s from the ground state energy E_0 when tilting the moment shown as two tilting angles. From the paraboloid surface fits in this figure, we determine the curvature ξ_{min} in Eq. (S9) in the Supplemental Material [29] and calculate the corresponding magnetic susceptibilities using Eq. (5). From this calculation, we can define the angle ratio ($d = \theta_{II}/\theta_I$, Eq. (S3) in the Supplemental Material [29]), explaining the magnetic structural details. Here, d values for Cr_2As, Mn_2As, and Fe_2As are 10.8, 0.26, and 1.01, respectively. Although the three materials

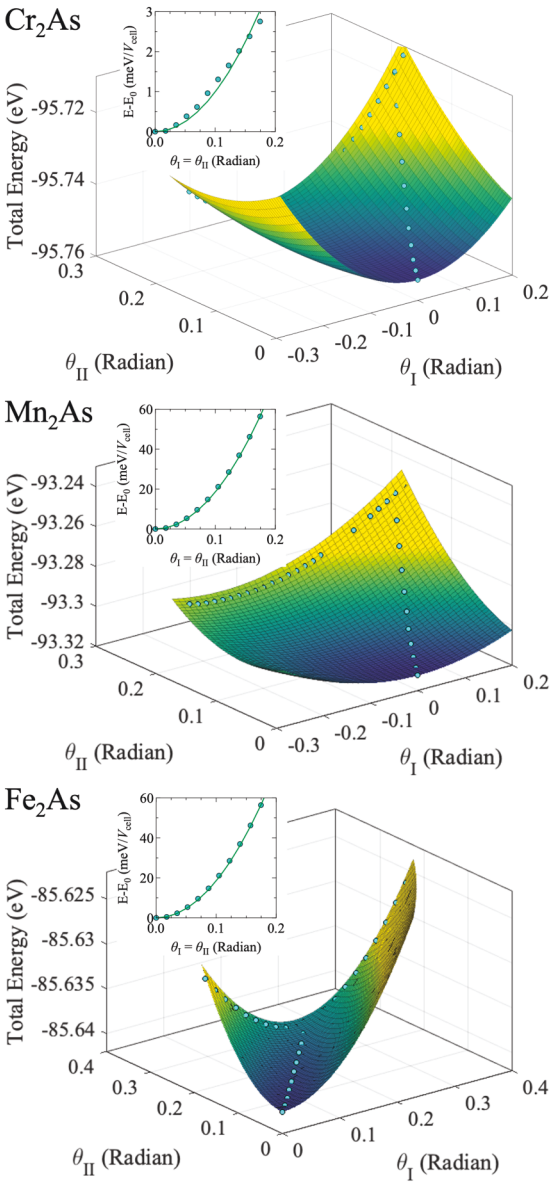

FIG. 3. Each cyan circle marker represents the total energy E_{tot} without the field term $\Delta E_B(\theta_{\text{I}}, \theta_{\text{II}})$ with respect to two angle changes at M(I) and M(II) sites for moment-tilted states of Cr_2As, Mn_2As, and Fe_2As. Colored surfaces show the fitted paraboloid in the form of Eq. (S2) in the Supplemental Material [29]. Insets present the total energy changes as a function of tilting angles with $\theta_{\text{I}} = \theta_{\text{II}}$ to compare the M_2As energy scales.

have similar AFM structures, their tilting behaviors are totally different. When we increase the external magnetic field, the moment tilting at the M(I) site is obviously smaller than that at the M(II) site in Cr_2As, while Mn_2As displays exactly the opposite behavior. Furthermore, the d value of Fe_2As is $\sim$1, meaning that the tilting angles at two magnetic sites are almost the same. Based on those tilted structures, our DFT results show that the perpendicular magnetic susceptibilities along the c axis of Cr_2As, Mn_2As, and Fe_2As are 3.08×10^{-4}, 5.34×10^{-4}, and 4.09×10^{-3}, respectively. The direct comparison between computational and experimental results is complicated by the unexpected temperature dependence of the measured susceptibilities for Mn_2As [39], Fe_2As [40], and Mn_3Sn [43]. To mitigate this unknown temperature-dependent effect, we compare the minimum value of the measure susceptibility between 0 K and the Néel temperature to the value of the magnetic susceptibility we calculate by DFT because the perpendicular magnetic susceptibility of ordinary AFMs at 0 K is close to the value of this minimum [41,42].

We also note that the energy change for a given z-axis magnetization is much smaller for Fe_2As than the other two materials based on the magnetic susceptibility results. The difference in magnitude of the magnetic susceptibilities of M_2As can be explained by their magnetic structures (see Fig. 2). Fe_2As has a unique magnetic structure in that each chemical unit cell is FM ordered, and the cells are layered with alternating antiparallel moment directions. Among the magnetic interactions in this structure, the FM exchange coupling does not largely contribute to magnetic susceptibility. This is because the magnetic configuration remains parallel with tilting, and the anisotropy energy contributions are small. Instead, the AFM coupling between layers is the main source of the exchange interaction energy change contributing to magnetic susceptibility since it is tilted against the antiparallel ground state orientation. Also, the calculated d values indicate that Fe_2As has almost parallel moments with FM interactions, while Mn_2As and Cr_2As show large moment tilting angle differences between two magnetic sites. With that fact, the effective exchange parameters, e.g., computed by Zhang *et al.* [36], show the total amount of AFM coupling in Fe_2As is smaller than that in Cr_2As and Mn_2As, causing its susceptibility to be larger than that of Cr_2As and Mn_2As. This also means that Fe_2As generates larger net magnetization along the field direction under a given external magnetic field, and we revisit this point later in our discussion of the PMOKE for different field strengths.

We want to estimate the applicability of the proposed magnetic susceptibility calculation method; thus, the magnetic susceptibilities of five metallic AFMs (MnPt [22], tetragonal CuMnAs, Mn_2Au, Cr_2Al [23], and Mn_3Sn) and one insulating AFM (MnF_2) in addition to M_2As are investigated. They can be grouped into various types of AFMs. MnPt is a uniaxial metallic AFM; tetragonal CuMnAs, Mn_2Au, and Cr_2Al are in-plane metallic AFMs with one magnetic site; Mn_3Sn is a noncollinear metallic AFM; and MnF_2 is a uniaxial insulating AFM. Since these materials have only one magnetic symmetric site, we used the method with a single tilting angle change. Calculated magnetic susceptibilities of MnPt [22], tetragonal CuMnAs, Mn_2Au, Cr_2Al [23], Mn_3Sn, and MnF_2 are 5.25×10^{-4}, 5.02×10^{-4}, 3.98×10^{-4}, 6.88×10^{-5}, 1.30×10^{-3}, and 8.63×10^{-3}, respectively. Figure 4 presents the comparison between measured and calculated magnetic susceptibilities. We report good agreement within 40% between our computational results and experimental data for AFM MnPt, tetragonal CuMnAs, Mn_2Au, Cr_2Al, and MnF_2. For MnF_2 [47] and Cr_2Al [23] as representatives of this set of materials, the experimentally reported temperature dependence of the parallel susceptibility for single crystals approaches zero at 0 K. Only polycrystalline samples were investigated for the other materials in this group [37,44–46]. Conversely, for collinear AFM Cr_2As, Mn_2As, Fe_2As and noncollinear AFM Mn_3Sn, we report larger differences of over 50%.

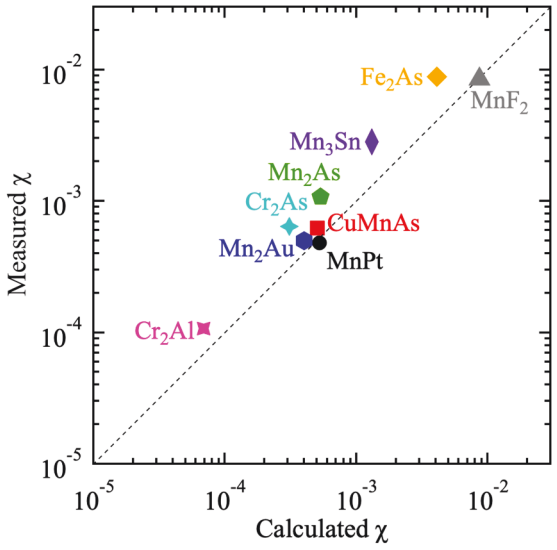

FIG. 4. The unitless magnetic susceptibilities comparison of metallic antiferromagnetic materials between the calculated and measured results. Measured values plotted in the figure originate from the reference of Cr_2As [37], Mn_2As [39], Fe_2As [40], MnPt [44], tetragonal CuMnAs [45], Mn_2Au [46], Cr_2Al [23], Mn_3Sn [43], and MnF_2 [47].

As mentioned in the previous paragraph, the perpendicular magnetic susceptibilities of Mn_2As [39] and Fe_2As [40] increase with cooling, caused by unknown thermal contributions. This behavior is also found in noncollinear AFM Mn_3Sn [43], which is expected to show temperature-independent magnetic susceptibility according to predictions using a Heisenberg model [48]. While the origin of this behavior remains unexplained and requires follow-up experiments and further modeling, we surmise that this complicates the comparison of the experimental susceptibility data to our 0 K computational results obtained for ideal crystals.

C. Band structure analysis

To understand how a PMOKE signal arises in AFM materials under an external magnetic field, we first explore the effect of such a field on the electronic band structure. We implement the tilted moment state calculation for a tilting angle varying from 0° to 10° at the M(II) site with the angle ratio d for $\xi_{\min}$ to describe the magnetic structure under the external magnetic field. For FM materials, Oppeneer *et al.* [12] discuss that essential parameters of the PMOKE are SOC, exchange splitting, and (strain-dependent) lattice spacing. The lattice relaxation due to moment tilting is <0.1% and, therefore, negligible. Hence, we focus on SOC and exchange splitting of electronic band structures, as illustrated in Fig. S1 in the Supplemental Material [29].

We define a measure $\Delta\bar{E}^{\mathrm{SOC}}$ for the spin-orbit splitting:

$$\Delta\bar{E}^{\mathrm{SOC}} = \sum_{\mathbf{k},i} \frac{|\varepsilon^{\mathrm{SOC}}(\mathbf{k},i) - \varepsilon^{\mathrm{noSOC}}(\mathbf{k},i)|}{N_k N_B}, \qquad (10)$$

where $\mathbf{k}$ indexes all N_k points in the Brillouin zone, and i is the band index running over all N_B bands. The dependence on N_B is weak, as shown in Fig. S2 in the Supplemental Material [29]. Kohn-Sham energies $\varepsilon^{\mathrm{SOC}}(\mathbf{k},i)$ and $\varepsilon^{\mathrm{noSOC}}(\mathbf{k},i)$ result from noncollinear DFT simulations with and without inclusion of the SOC effect, respectively [21], corresponding to the difference of band structures in Fig. S1(a) in the Supplemental Material [29]. Similarly, we quantify the effect of exchange splitting using

$$\Delta\bar{E}^{\mathrm{ES}} = \sum_{\mathbf{k},i} \frac{|\varepsilon^{\theta_{\mathrm{II}}}(\mathbf{k},i) - \varepsilon^{0^\circ}(\mathbf{k},i)|}{N_k N_B}, \qquad (11)$$

where $\varepsilon^{\theta_{\mathrm{II}}}(\mathbf{k},i)$ and $\varepsilon^{0^\circ}(\mathbf{k},i)$ are Kohn-Sham energies of the ith band at $\mathbf{k}$ for tilting of θ_{II} and 0°, respectively. While all bands of AFM materials are degenerate in the ground state, moment tilting leads to a net magnetization in the field direction and induces an exchange splitting (see the difference between band structures in Fig. S1(b) in the Supplemental Material [29]).

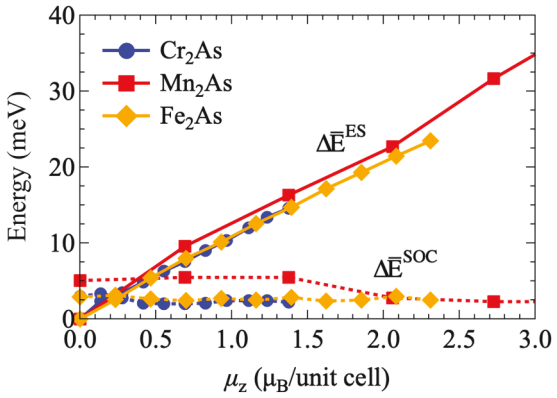

FIG. 5. Energy splittings $\Delta\bar{E}^{\mathrm{ES}}$, Eq. (11), and $\Delta\bar{E}^{\mathrm{SOC}}$, Eq. (10), vs magnetization for different tiltings of magnetic moments. Exchange splitting increases with magnetization, while spin-orbit coupling remains almost constant. Thus, we attribute the polar magneto-optical Kerr effect (PMOKE) signal change in antiferromagnetic M_2As under external magnetic fields to exchange splitting.

The resulting energy splittings $\Delta\bar{E}^{\mathrm{ES}}$ and $\Delta\bar{E}^{\mathrm{SOC}}$ are shown as a function of the magnetic moment tilting with the θ_{II} angle between 0° and 10° and corresponding θ_{I} angles in Fig. 5. This illustrates that increased tilting leads to increased net magnetization, while SOC is almost unaffected. At the same time, exchange splitting gradually increases for all three AFM M_2As materials. Thus, we conclude that the origin of the PMOKE signal change under external magnetic fields is purely due to the change of exchange splitting with tilting. We also note that the electronic band structure exhibits small spin-orbit-induced splitting even in the (untilted) AFM ground state. Hence, the vanishing PMOKE signal in the ground state is also explained exclusively by the absence of exchange splitting in this case. This interpretation is consistent with symmetry analysis which showed that the nonzero PMOKE occurs when the magnetic symmetry is broken by a nonzero net magnetization.

D. PMOKE

Tilting of magnetic moments affects the dielectric tensor, which directly determines the linear magneto-optical Kerr

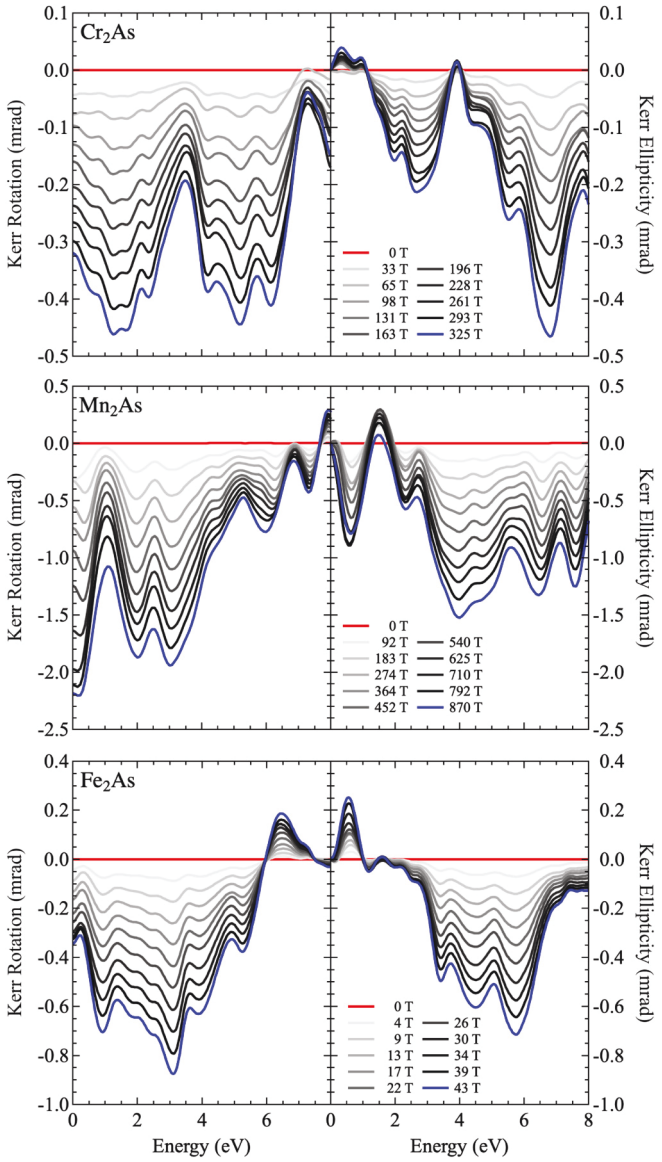

FIG. 6. Polar magneto-optical Kerr effect (PMOKE) rotation θ_K and ellipticity γ_K for antiferromagnetic Cr_2As, Mn_2As, and Fe_2As under external magnetic fields corresponding to the moment-tilting angle at the M(II) site θ_{II} from 0° to 10° in 1° increments with the corresponding θ_I via the angle ratio d. The magnetic field values are computed using the magnetic susceptibility from our density functional theory (DFT) results.

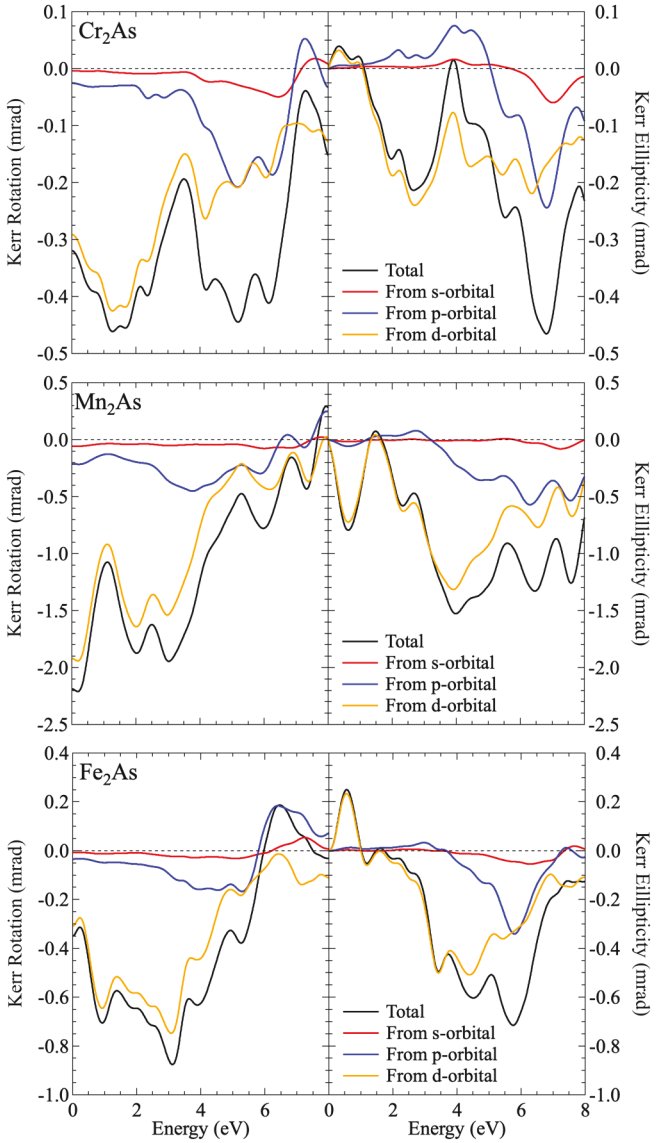

FIG. 7. Polar magneto-optical Kerr effect (PMOKE) rotation θ_K and ellipticity γ_K, decomposed in terms of the orbital angular momentum of the initial state, for antiferromagnetic Cr_2As, Mn_2As, and Fe_2As under an external magnetic field, corresponding to moment-tilting angles at the M(II) site (θ_{II}) of 10°.

tensor [10]. The $mmm1'$ point group does not allow for the linear MOKE by symmetry, while the dielectric tensor of the $m'm'm$ point group has off-diagonal elements that cause the linear MOKE via Eq. (6). We use Eq. (6) to compute PMOKE rotation θ_K and ellipticity γ_K from the complex frequency-dependent dielectric tensor of AFM M_2As under different magnetic moment tilting angles. Since most experimental MOKE studies are done in the visible spectral range, we use our data to report the wavelength that maximizes the MOKE signal in this range. The highest peaks of the Kerr rotation spectra plotted in Fig. 6 occur at 1.24 eV (Cr_2As), 0.18 eV (Mn_2As), and 3.10 eV (Fe_2As). In the case of Cr_2As and Mn_2As, these peaks are outside the visible spectral range between 1.66 and 3.30 eV, and the highest peaks within the visible spectrum occur at 1.66 and 3.00 eV. For Kerr ellipticity, the maxima occur at 6.80 eV (Cr_2As), 4.00 eV (Mn_2As), and 5.73 eV (Fe_2As), and the highest values in the visible spectral range are at 2.68, 3.30, and 3.30 eV, respectively. Using our computed magnetic susceptibility, magnetic moment tilting can be connected to the strength of the external magnetic field. Figure 6 illustrates a gradual increase of the PMOKE response as the external magnetic field increases. Peak positions and overall spectral shapes are almost unaffected by the field magnitude.

Furthermore, to understand characteristic peaks in M_2As PMOKE spectra, we decompose the electronic states with respect to atomic orbital contribution projections of each band state and check each orbital contribution. In Fig. 7, we present

the disentangled PMOKE spectra with respect to transitions from s, p, or d valence orbitals into all conduction band states. From these data, we show that transitions originating from metal d orbitals dominate the Kerr rotation energy range below ~5 eV for all three M_2As materials. At higher energies, these d contributions decrease and become comparable with contributions from p orbitals. These p states contribute most strongly for Cr_2As, where they are responsible for the Kerr rotation peaks at 5.17 and 6.15 eV. This feature does not occur for the other two compounds, explaining the difference in their MOKE spectra. The positive Kerr rotation signal contribution of p states and the small negative d state contribution happen as the sign changes at the high energy range in Mn_2As and Fe_2As. In Cr_2As, the negative signal contribution of the d state is still large, not causing the sign change of the Kerr rotation signal. All s electron contributions are weak for all three materials. Decomposing the d states into the different m contributions does not point to any dominating states.

Due to the small magnetic susceptibilities of Cr_2As, Mn_2As, and Fe_2As, moment tilting of only $\theta_{II} = 1^\circ$ and corresponding θ_I is still consistent with large external magnetic fields. At the same time, implementing small tilting angles using the constraint in Eq. (1) poses numerical challenges. Hence, we use the fact that the MOKE spectra depend linearly on the magnetic field for tilting (see Fig. 6) and linearly interpolate the response into the range of magnetic fields of practical importance. To this end, we compute the gradients $d\theta_K/dB$ and $d\gamma_K/dB$ for each photon energy, using the PMOKE spectra for tilted moments with the angle θ_{II} between 0° and 10° and corresponding θ_I, and the constraint of the vanishing PMOKE for $\theta_I = \theta_{II} = 0^\circ$ tilting. We then use these gradients to compute the PMOKE spectra for all three materials under an external magnetic field of 1 T, see Fig. 8. From this, we find that, while the PMOKE spectra exhibit a significant dependence on the photon energy, their overall magnitude is strongly influenced by the size of magnetic susceptibility ($Cr_2As < Mn_2As < Fe_2As$). The larger magnitude of the gradient observed for Fe_2As (see Fig. 8), compared with Cr_2As and Mn_2As, is due to the larger magnetic susceptibility of Fe_2As. Unlike FMs, AFMs suffer the moments tilting against exchange interaction under an external magnetic field. It causes small magnetic susceptibility and PMOKE signal changes over a wide range of applied external field strengths. Therefore, in addition to SOC and exchange splitting effect, magnetic susceptibility becomes another essential parameter to understand the PMOKE from AFM materials under external magnetic fields.

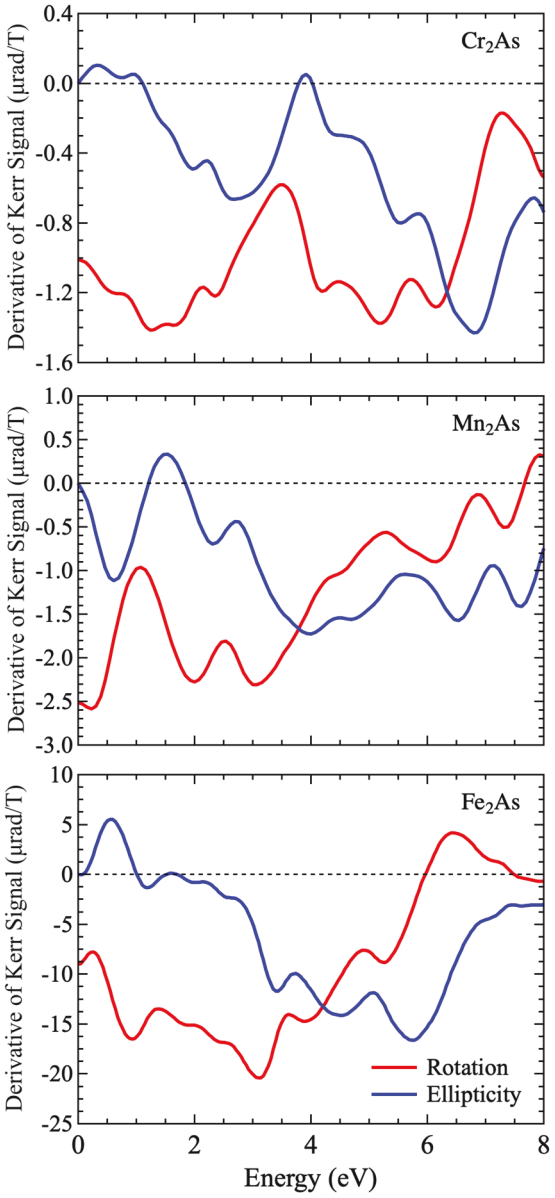

FIG. 8. Polar magneto-optical Kerr effect (PMOKE) signal gradient spectra $d\theta_K/dB$ (red solid lines) and $d\gamma_K/dB$ (blue solid lines) of antiferromagnetic M_2As which correspond to the PMOKE signal spectra under an external magnetic field of 1 T.

IV. CONCLUSIONS

Using first-principles electronic-structure simulations based on DFT, we predicted the PMOKE spectra for AFM M_2As (M = Cr, Mn, and Fe). Breaking of the magnetic symmetry is necessary for this effect to appear, and we simulate this via external magnetic fields that we implement using a constraint that tilts the magnetic moments. We devise a computational scheme to calculate magnetic susceptibility from the total energy change upon tilting and find reasonable agreement with experimental results in AFM materials, while M_2As materials and noncollinear AFM Mn_3Sn show somewhat deviating susceptibility values due to the unknown contributions that might originate from stoichiometry offset, site disorder, or paramagnetic defects.

Subsequently, we compute the frequency-dependent MOKE from the off-diagonal components of the dielectric tensor and study the dependence on the external field strength. Our simulation results show that the strength of Kerr rotation and ellipticity scales linearly. Using our band-structure results, we trace this back to exchange splitting and show that the dependence of the SOC effect on the external field is negligible. From our results, we conclude that SOC, exchange splitting, and magnetic susceptibility are three key parameters that jointly determine the MOKE in AFM materials under external

magnetic fields. Finally, we decompose the PMOKE spectra of M_2As into orbital contributions, showing that transitions from valence d orbitals are responsible for the PMOKE at energies <5 eV and from valenced orbitals cause the PMOKE >5 eV.

ACKNOWLEDGMENTS

This work was undertaken as part of the Illinois Materials Research Science and Engineering Center, supported by the National Science Foundation MRSEC program under NSF Award No. DMR-1720633. This paper is part of the Blue Waters sustained-petascale computing project, which is supported by the National Science Foundation (Awards No. OCI-0725070 and No. ACI-1238993) and the state of Illinois. Blue Waters is a joint effort of the University of Illinois at Urbana-Champaign and its National Center for Supercomputing Applications. This paper made use of the Illinois Campus Cluster, a computing resource that is operated by the Illinois Campus Cluster Program in conjunction with the National Center for Supercomputing Applications and which is supported by funds from the University of Illinois at Urbana-Champaign.

[1] J. Daughton, Thin Solid Films **216**, 162 (1992).
[2] S. Bhatti, R. Sbiaa, A. Hirohata, H. Ohno, S. Fukami, and S. Piramanayagam, Mater. Today **20**, 530 (2017).
[3] S. A. Siddiqui, J. Sklenar, K. Kang, M. J. Gilbert, A. Schleife, N. Mason, and A. Hoffmann, J. Appl. Phys. **128**, 040904 (2020).
[4] V. Baltz, A. Manchon, M. Tsoi, T. Moriyama, T. Ono, and Y. Tserkovnyak, Rev. Mod. Phys. **90**, 015005 (2018).
[5] P. Nemec, M. Fiebig, T. Kampfrath, and A. Kimel, Nat. Phys. **14**, 229 (2018).
[6] P. M. Oppeneer, Nat. Photonics **11**, 74 (2017).
[7] J. Kerr, London Edinburgh Dublin Philos. Mag. **3**, 321 (1877).
[8] C. Tzschaschel, K. Otani, R. Iida, T. Shimura, H. Ueda, S. Günther, M. Fiebig, and T. Satoh, Phys. Rev. B **95**, 174407 (2017).
[9] R. Iida, T. Satoh, T. Shimura, K. Kuroda, B. A. Ivanov, Y. Tokunaga, and Y. Tokura, Phys. Rev. B **84**, 064402 (2011).
[10] V. Eremenko, N. Kharchenko, Y. Litvinenko, and V. Naumenko, *Magneto-Optics and Spectroscopy of Antiferromagnets* (Springer, New York, 2012).
[11] K. Yang, K. Kang, Z. Diao, A. Ramanathan, M. H. Karigerasi, D. P. Shoemaker, A. Schleife, and D. G. Cahill, Phys. Rev. Materials **3**, 124408 (2019).
[12] P. M. Oppeneer, J. Sticht, T. Maurer, and J. Kübler, Z. Phys. B **88**, 309 (1992).
[13] Z. Wang, S. Kovalev, N. Awari, M. Chen, S. Germanskiy, B. Green, J.-C. Deinert, T. Kampfrath, J. Milano, and M. Gensch, Appl. Phys. Lett. **112**, 252404 (2018).
[14] Y. Yamaguchi, H. Watanabe, H. Yamauchi, and S. Tomiyoshi, J. Phys. Soc. Jpn. **32**, 958 (1972).
[15] A. E. Austin, E. Adelson, and W. H. Cloud, J. Appl. Phys. **33**, 1356S (1962).
[16] H. Katsuraki and N. Achiwa, J. Phys. Soc. Jpn. **21**, 2238 (1966).
[17] P. Hohenberg and W. Kohn, Phys. Rev. **136**, B864 (1964).
[18] G. Kresse and J. Furthmüller, Phys. Rev. B **54**, 11169 (1996).
[19] G. Kresse and D. Joubert, Phys. Rev. B **59**, 1758 (1999).
[20] M. Gajdoš, K. Hummer, G. Kresse, J. Furthmüller, and F. Bechstedt, Phys. Rev. B **73**, 045112 (2006).
[21] S. Steiner, S. Khmelevskyi, M. Marsmann, and G. Kresse, Phys. Rev. B **93**, 224425 (2016).
[22] K. Kang, D. G. Cahill, and A. Schleife, Phonon, electron, and magnon excitations in antiferromagnetic $L1_0$-type MnPt, arXiv:2112.13954 (2021).
[23] C. Zhao, K. Kang, J. C. Neuefeind, A. Schleife, and D. P. Shoemaker, Phys. Rev. Materials **5**, 084411 (2021).
[24] J. P. Perdew, K. Burke, and M. Ernzerhof, Phys. Rev. Lett. **77**, 3865 (1996).
[25] H. J. Monkhorst and J. D. Pack, Phys. Rev. B **13**, 5188 (1976).
[26] S. L. Dudarev, G. A. Botton, S. Y. Savrasov, C. J. Humphreys, and A. P. Sutton, Phys. Rev. B **57**, 1505 (1998).
[27] S. López-Moreno, A. H. Romero, J. Mejía-López, and A. Muñoz, Phys. Chem. Chem. Phys. **18**, 33250 (2016).
[28] The vasp Manual, 2019, https://www.vasp.at/wiki/index.php/I_CONSTRAINED_M.
[29] See Supplemental Material at http://link.aps.org/supplemental/10.1103/PhysRevB.105.184404 for the derivation of the equation for the magnetic susceptibility and the derivation of the electronic band structure.
[30] D. Sangalli, A. Marini, and A. Debernardi, Phys. Rev. B **86**, 125139 (2012).
[31] M. Veis, J. Minár, G. Steciuk, L. Palatinus, C. Rinaldi, M. Cantoni, D. Kriegner, K. K. Tikuišis, J. Hamrle, M. Zahradník, *et al.*, Phys. Rev. B **97**, 125109 (2018).
[32] H. Ehrenreich and M. H. Cohen, Phys. Rev. **115**, 786 (1959).
[33] J. Leveillee, C. Katan, L. Zhou, A. D. Mohite, J. Even, S. Tretiak, A. Schleife, and A. J. Neukirch, Phys. Rev. Materials **2**, 105406 (2018).
[34] H. T. Stokes and D. M. Hatch, J. Appl. Crystallogr. **38**, 237 (2005).
[35] H. T. Stokes, D. M. Hatch, and B. J. Campbell, ISOTROPY Software Suite, https://iso.byu.edu.
[36] Y. Zhang, J. Brgoch, and G. J. Miller, Inorg. Chem. **52**, 3013 (2013).
[37] M. Yuzuri, J. Phys. Soc. Jpn. **15**, 2007 (1960).
[38] M. Yuzuri and M. Yamada, J. Phys. Soc. Jpn. **15**, 1845 (1960).
[39] Y. Ishizawa and E. Hirahara, J. Phys. Soc. Jpn. **21**, 189 (1966).
[40] K. Yang, K. Kang, Z. Diao, M. H. Karigerasi, D. P. Shoemaker, A. Schleife, and D. G. Cahill, Phys. Rev. B **102**, 064415 (2020).
[41] C. Kittel, *Introduction to Solid State Physics* (Wiley, New York, 2004).
[42] N. W. Ashcroft and N. D. Mermin, *Solid State Physics* (Holt, Rinehart and Winston, Philadelphia, 1976).
[43] H. Ohmori, S. Tomiyoshi, H. Yamauchi, and H. Yamamoto, J. Magn. Magn. Mater. **70**, 249 (1987).
[44] R. Y. Umetsu, K. Fukamichi, and A. Sakuma, Mater. Trans. **47**, 2 (2006).

[45] K. Uhlířová, E. Duverger-Nédellec, R. H. Colman, J. Volný, B. Vondráčková, and K. Carva, J. Alloys Compd. **771**, 680 (2019).

[46] V. M. T. S. Barthem, C. V. Colin, H. Mayaffre, M. H. Julien, and D. Givord, Nat. Commun. **4**, 2892 (2013).

[47] R. Schleck, Y. Nahas, R. P. S. M. Lobo, J. Varignon, M. B. Lepetit, C. S. Nelson, and R. L. Moreira, Phys. Rev. B **82**, 054412 (2010).

[48] D. C. Johnston, Phys. Rev. Lett. **109**, 077201 (2012).